Improved $Sr_{0.6}La_{0.4}Co_{0.8}Fe_{0.2}O_{3−δ}$/$Ce_{0.8}Y_{0.2}O_{2−δ}$ interface for IT-SOFC applications

CrossMark

L. Baqué [a,*], K.P. Padmasree [b], M.A. Ceniceros Reyes [c], H. Troiani [a], A. Serquis [a], A. Soldati [a]

[a] CONICET, CAB-CNEA, Av. Bustillo 9500, (R8402AGP) S. C. de Bariloche, RN, Argentina
[b] CINVESTAV Unidad Saltillo, Apartado Postal 663, Saltillo, 25000, Mexico
[c] CIQA, Blvd. Enrique Reyna Hermosillo 140, Saltillo, 25294, Mexico

ARTICLE INFO

ABSTRACT

One of the remaining challenges for the solid oxide fuel cell (SOFC) technology is decreasing its operation temperature to the 500−800 °C range in a cost-effective way without diminishing the cell performance. In this work, we studied a symmetrical cell composed of $Sr_{0.6}La_{0.4}Co_{0.8}Fe_{0.2}O_{3−δ}$ (LSCFO) cathodes deposited on a $Ce_{0.8}Y_{0.2}O_{2−δ}$ (CYO) substrate by the simple, cost-effective and scalable spin coating technique. The nano-structured cathode is composed of agglomerated ~100−200 nm particles with ~50 nm crystallite size. Electrochemical impedance spectroscopy (EIS) analysis indicates that electrolyte grain boundary conductivity strongly depends on the cathode nature. The detailed high resolution transmission electron microscopy (HR-TEM) characterization of the LSCFO/CYO interface reveals that the LSCFO cathode is well adhered to the CYO electrolyte. The improved nano/microstructure of the cathodes and the cathode/electrolyte interface yields to cathode area specific resistance (ASR) values as low as 0.4 Ωcm^2 at 550 °C, being these values even lower than those previously reported in literature for cathodes in optimized LSCFO/CYO/YSZ/CYO/LSCFO cells.

Introduction

Solid oxide fuel cells (SOFCs) represent an efficient and environmentally friendly technology to convert directly the chemical energy of hydrogen and fossil fuels into electrical power and heat [1]. These devices require high operation temperature to allow the transport of oxygen ions through the ceramic components of the cell, challenging the long term stability and inducing rapid degradation of the cell [2]. The development of thin electrolytes as well as the use of new electrolyte materials allowed decreasing the operation temperature from 800−1000 °C to the 500−800 °C range in the so-called Intermediate Temperature (IT)-SOFCs [1,2]. Ceria-based oxides are one of the materials of choice for IT-SOFCs electrolytes because they present higher oxygen ion conductivities at lower operation temperatures than the conventionally used yttria stabilized zirconia (YSZ) electrolytes. $Ce_{1−x}Gd_xO_{2−δ}$ (CGO) is the most used ceria-based electrolyte with the highest ionic conductivity values among the doped-ceria family,
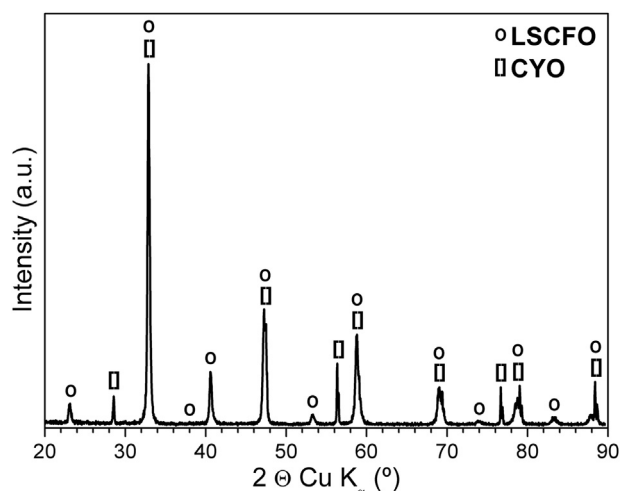
Fig. 1 – X-ray diffractogram collected at the cathode surface of the LSCFO/CYO/LSCFO cell.

values. The introduction of a CGO or CYO interlayer between the cathode and the zirconia-based electrolyte has been reported to be effective in preventing the formation of such detrimental phases and improving the cathode performance [17–19]. Interestingly, the cathode ASR values reported for symmetrical cells with a zirconia-based electrolyte and a ceria-based interlayer are at least 2 times lower than the values obtained for the same cathode deposited on an electrolyte with the same composition of the interlayer [19,20]. Despite these promising results, the incorporation of an interlayer implies a more intricate production process and higher associated costs. Therefore, research efforts are still necessary in order to obtain high performance cathodes with simple, straightforward, and cost-effective deposition methods.

In this work, we have studied the performance of nanostructured $Sr_{0.6}La_{0.4}Co_{0.8}Fe_{0.2}O_{3-\delta}$ cathodes deposited on a $Ce_{0.8}Y_{0.2}O_{2-\delta}$ electrolyte by the scalable and cost-effective spin coating technique. The constituent phases were identified by X-Ray Diffraction (XRD), while the microstructure was characterized by Scanning Electron Microscopy (SEM) and Transmission Electron Microscopy (TEM). The electrochemical response of this assembly was studied by Electrochemical Impedance Spectroscopy (EIS).

while $Ce_{1-x}Y_xO_{2-\delta}$ (CYO) represents a cost-effective alternative with ionic conductivity values in between those of CGO and YSZ [1,3].

The cathode area specific resistance (ASR) becomes significant as the SOFC operation temperature decreases, limiting the cell performance at intermediate temperatures [4]. The two main strategies to overcome this issue focus either on the use of cathode materials with enhanced transport and catalytic properties (i.e. mixed ionic-electronic conducting oxides and composites) [5–8] or on the development of nanostructured cathodes with large number of active sites for the oxygen reduction reaction (ORR) [9–12]. The more recently developed impregnated cathodes involve the two previously mentioned strategies [9,13,14]. A third approach consists in improving the cathode/electrolyte interface. For example, zirconia-based electrolytes can react with typical mixed conducting cathodes such as $La_{1-x}Sr_xCo_{1-y}Fe_yO_{3-\delta}$ (LSCFO) to form insulating phases (usually $La_2Zr_2O_7$ or $SrZrO_3$) [15,16] which hinder the oxygen ion conduction through the cathode/electrolyte interface, increasing the cathode ASR

Material and methods

$Ce_{0.8}Y_{0.2}O_{2-\delta}$ powders were prepared by the mechanical milling method [21,22] using CeO_2 and Y_2O_3 as starting materials and a milling time of 18 h. The obtained powders were uniaxially pressed with a pressure of 5 MPa to form pellets with ~10 mm diameter and ~1.1–1.4 mm thickness, and then sintered at 1500 °C for 5 h $Sr_{0.6}La_{0.4}Co_{0.8}Fe_{0.2}O_{3-\delta}$ powders were synthesized by an Acetate method reported elsewhere [11] and sintered in air at 800 °C for 6 h. These powders were dispersed in a mixture of isopropyl alcohol, terpineol, polyvinyl butyral (PVB), and polyvinyl pyrridone (PVP) with a powder:alcohol:terpineol:PVB:PVP weight ratio of 35:38.8:23.6:1.7:0.9 obtaining an ink with a viscosity of ~130 cP. This ink was deposited at room temperature onto both sides of a CYO substrate by the spin coating technique with a spinning
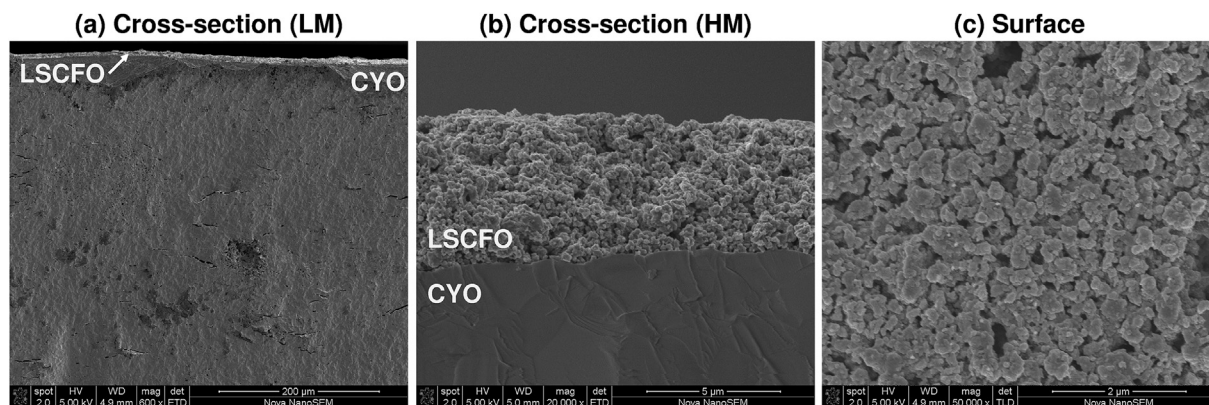

Fig. 2 – (a) Cross-section (Low Magnification), (b) cross-section (High Magnification), and (b) surface SEM images of the LSCFO/CYO/LSCFO cell.

speed of 4000 rpm and a spinning time of 20 s. Each cathode completely covered the electrolyte surface having all a geometric planar area (A) of ~0.95 cm^2. Afterwards, this assembly was heat treated in air at 900 °C for 6 h, resulting in a symmetrical cell configuration used for electrochemical measurements. Separately, both sides of a CYO substrate were painted with Pt paste and then heat treated in air at 800 °C for 2 h. This symmetrical cell was used to determine the electrolyte contribution to the impedance spectra.

The LSCFO/CYO/LSCFO symmetrical cell was characterized by XRD, SEM and TEM. XRD measurements were performed on the cell surface at room temperature using a Philips PW1700 diffractometer with Cu K$_\alpha$ radiation and a graphite monochromator. Diffractograms were collected over the 20° ≤ 2Θ ≤ 90° range with 0.025° step and 1 s/step counting time. Average crystallite size was estimated by Scherrer formula [23]. LSCFO/CYO/LSCFO cell was mechanically fractured and mounted in a SEM sample holder in order to observe its

surface and cross-section by using a FEI Nova NanoSEM 230 scanning electron microscope. Thicknesses and particle sizes were determined manually by using the ImageJ software [24]. TEM site-specific lamella including the cathode/electrolyte interface were prepared by a Dual beam SEM/FIB (Focused Ion Beam) Quanta 200 3D microscope from FEI where a thin Pt-layer was deposited on the surfaces of the selected areas to protect the underlying material from the milling process. Rough cuts were carried out with an acceleration voltage of 30 kV and 5 nA while the final thinning was achieved at 10 kV and 50 pA. TEM and HR-TEM images were obtained using a Philips CM 200 UT microscope equipped with an ultra-twin objective lens. The electron source used was a LaB$_6$ filament operated at 200 keV. The nominal resolution was 0.2 nm for high resolution mode. EIS measurements were performed on both LSCFO/CYO/LSCFO and Pt/CYO/Pt symmetrical cells in the 100–550 °C temperature range under pure oxygen. Impedance spectra were recorded using a potentiostast/
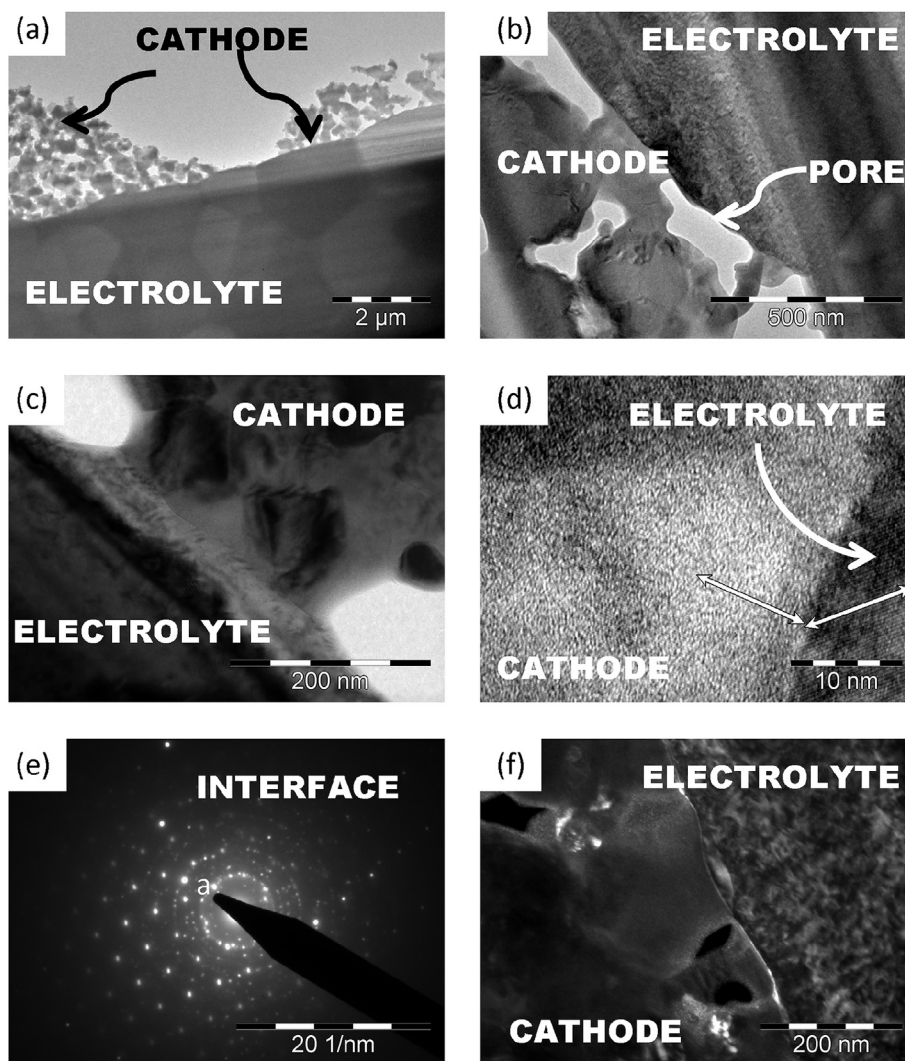
Fig. 3 — (a) TEM image of the cell assembly. (b) Magnification at the interface. Pores and zones of excellent adhesion can be observed. (c) Bright Field TEM image showing the interface with higher contrast. (d) High resolution (HR)-TEM image of the cathode/electrolyte interface; the white arrows indicate the atomic planes orientation. (e) Selected Area Electron diffraction pattern of the cathode/electrolyte interface. (f) Dark Field image done with points that belong to both phases (indicated with "a" in Fig. (e)).

(a)

(b)

(c)
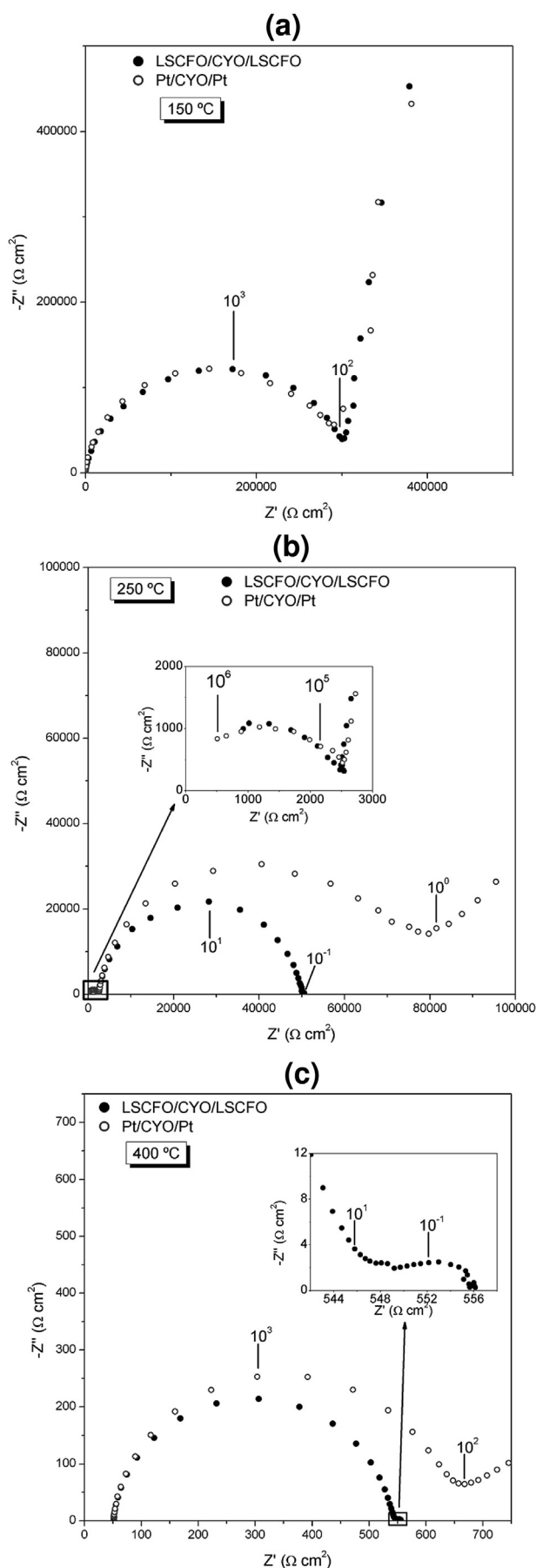
impedance analyzer Autolab (Eco Chemie BV) within 10^{-3}–10^6 Hz frequency range. Gold grids, slightly pressed on electrodes, were used as current collectors. All spectra were fitted using the software ZView 2.8d [25].

Results and discussion

Microstructural characterization

XRD data collected at the cathode surface of the LSCFO/CYO/LSCFO cell are shown in Fig. 1. All the peaks can be identified as belonging to the LSCFO phase (PDF card 00-048-0124) or the CYO phase (PDF card 01-075-0175). The absence of any other phase indicates that there was no chemical reaction between the cathode and the electrolyte. Crystallite size is ~50 nm for the LSCFO phase, while it is larger than the maximum detectable crystallite size for the CYO phase.

Fig. 2 displays SEM images from the cross-section and the surface of the LSCFO/CYO/LSCFO cell. In Fig. 2a and b, LSCFO cathode is the porous layer at the top with a thickness of ~5 μm while CYO electrolyte is the fully dense substrate at the bottom. It can be also observed that the cathode is composed of agglomerated ~100–200 nm particles with a homogenously distributed fine porosity (see Fig. 2b and c).

A FIB lamella containing the interface between the cathode layer and the electrolyte was analyzed by TEM (Fig. 3). The cathode can be recognized as a nanoparticulated material and the electrolyte presents micrometric grains and high density (Fig. 3a). The interface is composed of well-connected zones and pores (Fig. 3b). The first ones are observed in Fig. 3c and d. The high resolution images show an orientation relationship of 120° between the atomic orientation of the cathode and the electrolyte. Between both phases, no other materials (such as parasitic secondary phases) or signs of degradation or amorphization are observed. Indeed, a selected area electron diffraction (SAED) pattern obtained at the interface (Fig. 3e) shows two kind of patterns: a single crystal pattern corresponding to the CYO grain and a polycrystalline one, composed of concentric circles that corresponds to the nanocrystalline cathode. A Dark Field image (Fig. 3f) done with the diffraction point "a" in Fig. 3e produces signals in both the cathode and the electrolyte. Similar situations were reported in CGO/LSCFO assemblies [26].

Electrochemical impedance spectroscopy

Typical impedance spectra recorded at different temperatures for the LSCFO/CYO/LSCFO and Pt/CYO/Pt cells are shown in Fig. 4. At low temperatures, a complete arc starting at the origin of the coordinate axes can be observed along with part of a second arc located at intermediate frequencies (see Fig. 4a). As the temperature increases, a third arc starts to be

Fig. 4 – Nyquist plot of EIS spectra for the LSCFO/CYO/LSCFO and Pt/CYO/Pt symmetrical cells recorded under pure oxygen at (a) 150 °C, (b) 250 °C, and (c) 400 °C. EIS spectra were normalized by the cathode area divided by 2. The numbers indicate the frequency in Hz.

(a)

(b)

(c)
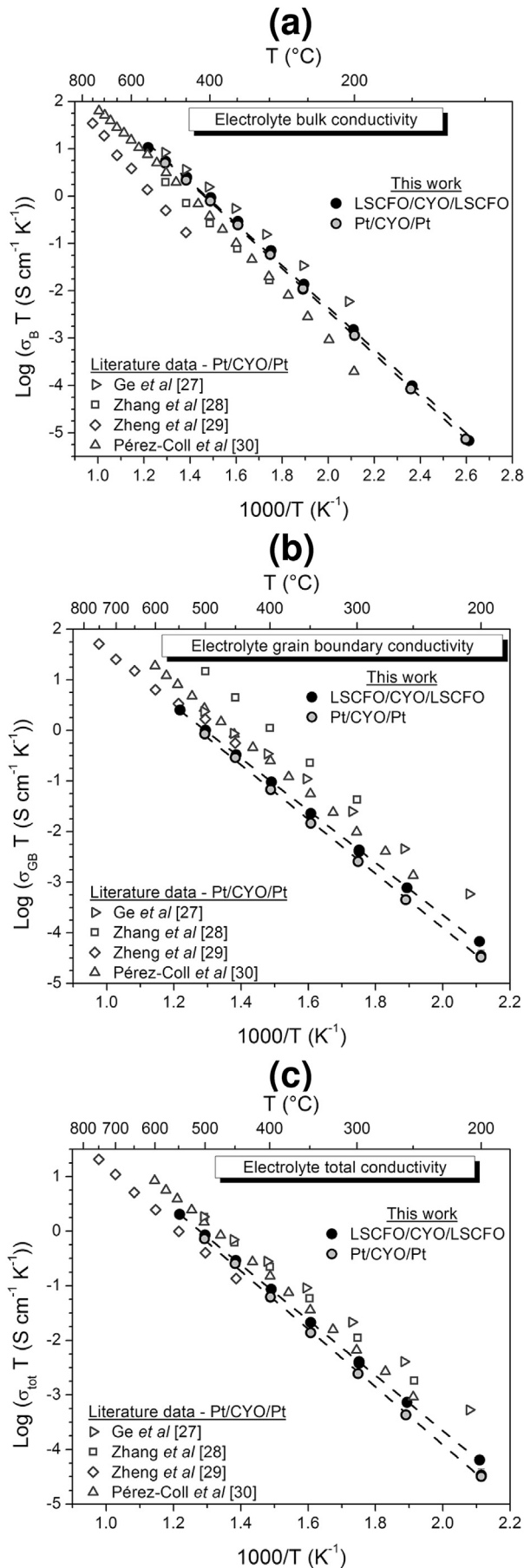
observed at low frequencies (see Fig. 4b). The high frequency arc shifts to frequencies above the measuring range for temperatures higher than 300 °C (see Fig. 4c), and the low frequency arc becomes fully distinguishable (see inset in Fig. 4c). In the literature, the high frequency contribution is generally attributed to the oxygen ion conductivity throughout the electrolyte bulk, the intermediate frequency contribution is associated to the grain boundary conduction, and the low frequency contribution is ascribed to the oxygen reduction reaction at the cathode [27—32].

Conductivity values (σ_i) were estimated by $\sigma_i = L/(R_i \, A)$ where L is the electrolyte thickness, R_i is the resistance of each contribution estimated by fitting the EIS spectra, and A is the geometric area of the electrolyte. The resistances of the bulk and grain boundary contributions were estimated by fitting the high frequency and the intermediate frequency arcs with two R//CPE subcircuits connected in series, being each subcircuit composed of a resistance (R) in parallel with a constant phase element (CPE). In the case of the total electrolyte conductivity, R_i is defined as the sum of the bulk and the grain boundary resistances. Fig. 5 shows the Arrhenius plots of the bulk, grain boundary and total conductivity values of the CYO electrolyte corresponding to the LSCFO/CYO/LSCFO and the Pt/CYO/Pt cells. For comparison, some results previously reported in literature for symmetrical cells with $Ce_{0.8}Y_{0.2}O_{2-\delta}$ electrolytes and Ag [27—29] or Pt electrodes [30] are also included. Bulk conductivity values are practically the same for LSCFO/CYO/LSCFO and Pt/CYO/Pt cells. In contrast, grain boundary conductivity values are ~1.1—2 times higher for the LSCFO/CYO/LSCFO cell indicating that the grain boundary conductivity is noticeably influenced by the electrode nature. This is in agreement with the findings of Duncan et al. [33], who observed that the grain boundary conductivity values of CGO electrolytes strongly depend on the composition and microstructure of the electrodes while the bulk conductivity values are not affected. Bulk and total conductivity values obtained for the LSCFO/CYO/LSCFO and the Pt/CYO/Pt cells are among those reported for $Ce_{0.2}Y_{0.8}O_{2-\delta}$ electrolytes, while grain boundary conductivity values are within the lowest ones. Some scatter between the electrolyte conductivity values reported by different authors is expected to occur, since they are determined by several factors. Bulk conductivity is mainly influenced by the electrolyte porosity, while grain boundary conductivity is mostly affected by the electrolyte porosity, the grain size and the presence of impurities [34—36]. The capacitance values for the high frequency arc are within the $7.8 \times 10^{-11} - 1.3 \times 10^{-10} \, F/cm^2$ range for the Pt/CYO/Pt cell and within the $5.2 \times 10^{-11} - 6.4 \times 10^{-11} \, F/cm^2$ range for the LSCFO/CYO/LSCFO cell, while those corresponding to the intermediate frequency arc are within the $2.3 \times 10^{-8} - 3.9 \times 10^{-8} \, F/cm^2$ range for the Pt/CYO/Pt cell and within the $2.9 \times 10^{-8} - 3.3 \times 10^{-8} \, F/cm^2$ range for the LSCFO/CYO/LSCFO

Fig. 5 — Arrhenius plots of (a) bulk, (b) grain boundary and (c) total conductivity values of the electrolyte measured under pure oxygen for the LSCFO/CYO/LSCFO and Pt/CYO/Pt cells. The dotted lines represent the linear fitting of values. Data from literature [27—30] is also displayed.

cell. These capacitance values of the high frequency arc are within those reported in the literature for bulk conduction through CYO electrolytes, whereas the capacitance values corresponding to the intermediate frequency arc are within those reported for grain boundary conduction [30,37]. Based on all the above, the high frequency and the intermediate frequency contributions of the impedance spectra can be safely assigned to electrolyte bulk and grain boundary conductivities, respectively.

Cathode area specific resistance ($ASR_{cathode}$) values were determined with the procedure described in Ref. [38] and plotted in Fig. 6. Data from several symmetrical cells with different configurations previously reported by other authors [39–41] are also shown. Our $Sr_{0.6}La_{0.4}Co_{0.8}Fe_{0.2}O_{3-\delta}$/ $Ce_{0.8}Y_{0.2}O_{2-\delta}$/$Sr_{0.6}La_{0.4}Co_{0.8}Fe_{0.2}O_{3-\delta}$ cell presents the lowest $ASR_{cathode}$ values (closed star symbol) in the 400–550 °C temperature range with an activation energy of 1.1 ± 0.1 eV. These $ASR_{cathode}$ values are ~30 times lower than those reported for a LSCFO/CYO/LSCFO cell (circle symbol) [39] and ~4–8 times smaller than those reported for a LSCFO/CYO/ YSZ/CYO/LSCFO cell (triangle symbol) [40], both cells having iron-rich $La_{0.6}Sr_{0.4}Co_{0.2}Fe_{0.8}O_{3-\delta}$ cathodes. Such a noticeable reduction in $ASR_{cathode}$ values can be originated in the different cathode composition since cobalt-rich oxides of the $La_{1-x}Sr_xCo_{1-y}Fe_yO_{3-\delta}$ family usually exhibit better catalytic properties for ORR than those rich in iron [42]. Nevertheless, the $ASR_{cathode}$ values of the LSCFO/CYO/YSZ/CYO/LSCFO cell with iron-rich cathodes are similar than those reported for a symmetrical cell with the same configuration but having $La_{0.6}Sr_{0.4}CoO_{3-\delta}$ (square symbol) [41] cathodes. This indicates that the microstructure of the cathode and the cathode/ electrolyte interface plays a more significant role than composition. Moreover, our cell present $ASR_{cathode}$ values that are up to ~3 times lower than those obtained for an optimized cell configuration fabricated by adding a dense LSCFO interlayer between the porous LSCFO cathode and the CYO interlayer (diamond symbol) [40]. It is worth to note that even though the use of interlayers between the cathode and the electrolyte usually improves the cathode performance, it involves a more complicated and expensive fabrication

process. In contrast, our LSCFO/CYO/LSCFO symmetrical cells with no interlayer between cathode and electrolyte were prepared by a simple and scalable procedure with the benefit of having the $ASR_{cathode}$ values as low as 0.4 Ωcm^2 at 550 °C. Such low $ASR_{cathode}$ values are a result of the optimal cathode nanostructure (containing high density of active sites for the oxygen reduction reaction) along with the well adhered cathode/electrolyte interface (without the presence of secondary phases) which facilitates the oxygen ion transfer from cathode to electrolyte.

Conclusions

A detailed and combined structural, microstructural and electrochemical investigation of a LSCFO/CYO/LSCFO symmetrical cell with nanostructured cathodes was performed by EIS, XRD, SEM, and TEM. EIS spectra present three contributions, namely the bulk and grain conduction through the electrolyte and the oxygen reduction reaction at the cathode. The comparison of LSCFO/CYO/LSCFO cell results with those of a Pt/CYO/Pt cell indicates that electrolyte grain boundary conductivity depends on the nature of the electrode, while the electrolyte bulk conductivity is not affected. Cathode nanostructure is composed of agglomerated ~100–200 nm particles with ~50 nm crystallite size according to the SEM and XRD analyses. HR-TEM observations at the cathode/electrolyte interface reveal an excellent adhesion between the LSCFO cathode and the CYO electrolyte without the presence of detrimental secondary phases. The interlayer-free LSCFO/ CYO/LSCFO symmetrical cell reported here presents an improved nano/microstructure of the cathode and the cathode/electrolyte interface which allowed obtaining $ASR_{cathode}$ values as low as 0.4 Ωcm^2 at 550 °C. These values are even lower than those reported in the literature for cathodes in LSCFO/CYO/LSCFO and optimized LSCFO/CYO/YSZ/CYO/ LSCFO symmetrical cells which require more intricate and costly fabrication processes. In conclusion, the results reported here clarify the significant role of a clean and well
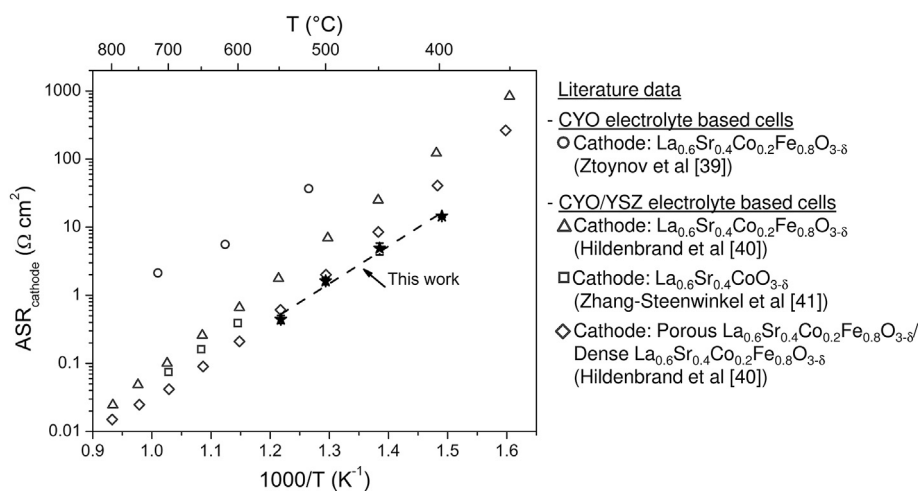

Fig. 6 – Arrhenius plots of the cathode ASR values measured under pure oxygen for the LSCFO/CYO/LSCFO cell. The dotted line represents the linear fitting of values. Data from literature [39–41] is also displayed.

adhered cathode/electrolyte interface for IT-SOFC applications.

Acknowledgments

REFERENCES

[1] Brett DJL, Atkinson A, Brandon NP, Skinner SJ. Intermediate temperature solid oxide fuel cells. Chem Soc Rev 2008;37:1568—78. http://dx.doi.org/10.1039/b612060c.

[2] Wachsman ED, Lee KT. Lowering the temperature of solid oxide fuel cells. Science 2011;334:935—9. http://dx.doi.org/10.1126/science.1204090.

[3] Wincewicz KC, Cooper JS. Taxonomies of SOFC material and manufacturing alternatives. J Power Sources 2005;140:280—96. http://dx.doi.org/10.1016/j.jpowsour.2004.08.032.

[4] Ivers-Tiffée E, Weber A, Herbstritt D. Materials and technologies for SOFC components. J Eur Ceram Soc 2001;21:1805—11. http://dx.doi.org/10.1016/S0955-2219(01)00120-0.

[5] Sun C, Hui R, Roller J. Cathode materials for solid oxide fuel cells: a review. J Solid State Electrochem 2010;14:1125—44. http://dx.doi.org/10.1007/s10008-009-0932-0.

[6] Tsipis EV, Kharton VV. Electrode materials and reaction mechanisms in solid oxide fuel cells: a brief review. III. Recent trends and selected methodological aspects. J Solid State Electrochem 2011;15:1007—40. http://dx.doi.org/10.1007/s10008-011-1341-8.

[7] Chen Y, Zhou W, Ding D, Liu M, Ciucci F, Tade M, et al. Advances in cathode materials for solid oxide fuel cells: complex oxides without alkaline earth metal elements. Adv Energy Mater 2015;5:1500537. http://dx.doi.org/10.1002/aenm.201500537.

[8] Gwon O, Yoo S, Shin J, Kim G. Optimization of $La_{1-x}Sr_xCoO_{3-\delta}$ perovskite cathodes for intermediate temperature solid oxide fuel cells through the analysis of crystal structure and electrical properties. Int J Hydrogen Energy 2014;39:20806—11. http://dx.doi.org/10.1016/j.ijhydene.2014.07.137.

[9] Lee KT, Wachsman ED. Role of nanostructures on SOFC performance at reduced temperatures. MRS Bull 2014;39:783—91. http://dx.doi.org/10.1557/mrs.2014.193.

[10] Hayd J, Yokokawa H, Ivers-Tiffée E. Hetero-interfaces at nanoscaled $(La,Sr)CoO_{3-\delta}$ thin-film cathodes enhancing oxygen surface-exchange properties. J Electrochem Soc 2013;160:F351—9. http://dx.doi.org/10.1149/2.017304jes.

[11] Baqué L, Caneiro A, Moreno MS, Serquis A. High performance nanostructured IT-SOFC cathodes prepared by novel chemical method. Electrochem Commun 2008;10:1905—8. http://dx.doi.org/10.1016/j.elecom.2008.10.010.

[12] Evans A, Martynczuk J, Stender D, Schneider CW, Lippert T, Prestat M. Low-temperature micro-solid oxide fuel cells with partially amorphous $La_{0.6}Sr_{0.4}CoO_{3-\delta}$ cathodes. Adv Energy Mater 2015;5:1400747. http://dx.doi.org/10.1002/aenm.201400747.

[13] Ding D, Lai SY, Gerdes K, Liu M. Enhancing SOFC cathode performance by surface modification through infiltration. Energy Environ Sci 2014;7:552—75. http://dx.doi.org/10.1039/c3ee42926a.

[14] Burye TE, Nicholas JD. Improving $La_{0.6}Sr_{0.4}Co_{0.8}Fe_{0.2}O_{3-\delta}$ infiltrated solid oxide fuel cell cathode performance through precursor solution desiccation. J Power Sources 2015;276:54—61. http://dx.doi.org/10.1016/j.jpowsour.2014.11.082.

[15] Martínez-Amesti A, Larrañaga A, Rodríguez-Martínez LM, Aguayo AT, Pizarro JL, Nó ML, et al. Reactivity between La(Sr)FeO₃ cathode, doped CeO_2 interlayer and yttria-stabilized zirconia electrolyte for solid oxide fuel cell applications. J Power Sources 2008;185:401—10. http://dx.doi.org/10.1016/j.jpowsour.2008.06.049.

[16] Kostogloudis GCh, Tsiniarakis G, Ftikos Ch. Chemical reactivity of perovskite oxide SOFC cathodes and yttria stabilized zirconia. Solid State Ionics 2000;135:529—35. http://dx.doi.org/10.1016/S0167-2738(00)00433-1.

[17] Constantin G, Rossignol C, Briois P, Billard A, Dessemond L, Djurado E. Efficiency of a dense thin CGO buffer layer for solid oxide fuel cell operating at intermediate temperature. Solid State Ionics 2013;249—250:98—104. http://dx.doi.org/10.1016/j.ssi.2013.07.004.

[18] Peña-Martínez J, Marrero-López D, Sánchez-Bautista C, Dos Santos-García AJ, Ruiz-Morales JC, Canales-Vazquez J, et al. Effect of a CGO buffer layer on the performance of $(La_{0.6}Sr_{0.4})_{0.995}Co_{0.2}Fe_{0.8}O_{3-\delta}$ cathode in YSZ-based SOFC. Bol Soc Esp Ceram 2010;49:15—22.

[19] Charojrochkul S, Choy K-L, Steele BCH. Cathode/electrolyte systems for solid oxide fuel cells fabricated using flame assisted vapour deposition technique. Solid State Ionics 1999;121:107—13. http://dx.doi.org/10.1016/S0167-2738(98)00536-0.

[20] Shiono M, Kobayashi K, Nguyen TL, Hosoda K, Kato T, Ota K, et al. Effect of CeO_2 interlayer on ZrO_2 electrolyte/La(Sr)CoO₃ cathode for low-temperature SOFCs. Solid State Ionics 2004;170:1—7. http://dx.doi.org/10.1016/j.ssi.2004.02.018.

[21] Padmasree KP, Montalvo-Lozano RA, Montemayor SM, Fuentes AF. Electrical conduction and electric relaxation process in $Ce_{0.8}Y_{0.2}O_{1.9}$ electrolyte system. J Alloys Compd 2011;509:8584—9. http://dx.doi.org/10.1016/j.jallcom.2011.06.036.

[22] Montalvo-Lozano RA, Montemayor SM, Padmasree KP, Fuentes AF. Effect of Ca^{2+} and Mg^{2+} additions on the electrical properties of yttria doped ceria electrolyte system. J Alloys Compd 2012;525:184—90. http://dx.doi.org/10.1016/j.jallcom.2012.02.045.

[23] Scherrer P. Bestimmung der grösse und der inneren struktur von kolloidteilchen mittels röntgenstrahlen. Nachr Ges Wiss Göttingen 1918;26:98—100.

[24] Rasband WS. ImageJ, U.S. National institutes of health. Bethesda, Maryland, USA. 1997-2014. http://imagej.nih.gov/ij.

[25] Associates Scribner. ZView for Windows, version 2.8d. 2005.

[26] Soldati AL, Baqué L, Troiani H, Cotaro C, Schreiber A, Caneiro A, et al. High resolution FIB-TEM and FIB-SEM characterization of electrode/electrolyte interfaces in solid oxide fuel cells materials. Int J Hydrogen Energy 2011;36:9180—8. http://dx.doi.org/10.1016/j.ijhydene.2011.04.121.

[27] Ge L, Li S, Zheng Y, Zhou M, Chen H, Guo L. Effect of zinc oxide doping on the grain boundary conductivity of $Ce_{0.8}Ln_{0.2}O_{1.9}$ ceramics (Ln = Y, Sm, Gd). J Power Sources 2011;196:6131—7. http://dx.doi.org/10.1016/j.jpowsour.2011.03.032.

[28] Zhang TS, Ma J, Huang HT, Hing P, Xia ZT, Chan SH, et al. Effects of dopant concentration and aging on the electrical properties of Y-doped ceria electrolytes. Solid State Sci 2003;5:1505—11. http://dx.doi.org/10.1016/j.solidstatesciences.2003.10.001.

[29] Zheng Y, Wu L, Gu H, Gao L, Chen H, Guo L. The effect of Sr on the properties of Y-doped ceria electrolyte for IT-SOFCs. J Alloys Compd 2009;486:586—9. http://dx.doi.org/10.1016/j.jallcom.2009.07.011.

[30] Pérez-Coll D, Marrero-López D, Núñez P, Piñol S, Frade JR. Grain boundary conductivity of $Ce_{0.8}Ln_{0.2}O_{2-\delta}$ ceramics (Ln = Y, La, Gd, Sm) with and without Co-doping. Electrochimica Acta 2006;51:6463—9. http://dx.doi.org/10.1016/j.electacta.2006.04.032.

[31] Baqué L, Soldati A, Troiani H, Schreiber A, Caneiro A, Serquis A. Enhaced oxygen reduction reaction kinetics in nanocrystalline IT-SOFC cathodes. ECS Trans 2013;57:2147—56. http://dx.doi.org/10.1149/05701.2147ecst.

[32] Baqué L, PhD Thesis, Instituto Balseiro-UNCuyo, 2011, (available online at:http://ricabib.cab.cnea.gov.ar).

[33] Duncan H, Lasia A. Influence of the electrode nature on conductivity measurements of gadolinia-doped ceria. Solid State Ionics 2005;176:1429—37. http://dx.doi.org/10.1016/j.ssi.2005.03.018.

[34] Pérez-Coll D, Sánchez-López E, Mather GC. Influence of porosity on the bulk and grain-boundary electrical properties of Gd-doped ceria. Solid State Ionics 2010;181:1033—42. http://dx.doi.org/10.1016/j.ssi.2010.06.006.

[35] Tadokoro SK, Muccillo ENS. Influence of the precursor purity and the precipitating agent on impedance spectroscopy of $CeO_2:Y_2O_3$ ceramics. J Alloys Compd 2004;374:190—3. http://dx.doi.org/10.1016/j.jallcom.2003.11.090.

[36] Christie GM, van Berkel FPF. Microstructure — ionic conductivity relationships in ceria-gadolinia electrolytes. Solid State Ionics 1996;83:17—27. http://dx.doi.org/10.1016/0167-2738(95)00155-7.

[37] Yan PF, Mori T, Suzuki A, Wu YY, Auchterlonie GJ, Zou J, et al. Grain boundary's conductivity in heavily yttrium doped ceria. Solid State Ionics 2012;222—223:31—7. http://dx.doi.org/10.1016/j.ssi.2012.06.026.

[38] Baqué L, Djurado E, Rossignol C, Marinha D, Caneiro A, Serquis A. Electrochemical performance of nanostructured IT-SOFC cathodes with different morphologies. ECS Trans 2009;25:2473—80. http://dx.doi.org/10.1149/1.3205802.

[39] Stoynov Z, Vladikova D, Raikova G, Soysal D, Ilhan Z, Ansar S. Impedance behavior of LSCF/YDC/LSCF symmetrical half cell prepared by plasma spray. In: Vladikova D, Stoynov Z, editors. Proceedings of the international workshop "Advances and innovations in SOFCs". Sofia: Institute of Electrochemistry and Energy Systems — Bulgarian Academy of Sciences; 2009. p. 77—82.

[40] Hildenbrand N, Boukamp BA, Nammensma P, Blank DHA. Improved cathode/electrolyte interface of SOFC. Solid State Ionics 2011;192:12—5. http://dx.doi.org/10.1016/j.ssi.2010.01.028.

[41] Zhang-Steenwinkel Y, van Tuel MMA, van Berkel FPF, Rietveld G. Development of novel cell components for low-temperature SOFC. ECS Trans 2007;7:271—8. http://dx.doi.org/10.1149/1.2729101.

[42] Takeda Y, Kanno R, Noda M, Tomida Y, Yamamoto O. Cathodic polarization phenomena of perovskite oxide electrodes with stabilized zirconia. J Electrochem Soc 1987;134:2656—61. http://dx.doi.org/10.1149/1.2100267.